Full-Length Paper Protein Science

DOI10.1002/pro.4273

A Favorable Path to Domain Separation in the Orange Carotenoid Protein

Mahmoud Sharawy [1], Natalia B. Pigni [2,3], Eric R. May [1*], and José A. Gascón [2*]

[1] Department of Molecular and Cell Biology, University of Connecticut, Storrs, Connecticut 06269-3125, USA
[2] Department of Chemistry, University of Connecticut, Storrs, Connecticut 06269-3060, USA
[3] Instituto de Ciencia y Tecnología de Alimentos Córdoba (ICYTAC-CONICET), Ciudad Universitaria, Córdoba X5000HUA, Argentina

Corresponding Authors
[*] José A. Gascón (jose.gascon@uconn.edu), 55 N. Eagleville Rd, Storrs, CT 06269, Phone: (860) 486-0591, Fax: (860) 486-2981
[*] Eric R. May (eric.may@uconn.edu), 91 North Eagleville Road, Unit 3125, Storrs, CT 06269, Phone: (860) 486-0484, Fax: (860) 486-4331

Running Title
Path to domain dissociation in OCP

Number of manuscript pages: 35 (including this one)

Number of supplementary material pages: 12

Number of tables' pages: 1

Number of figures' pages: 8 (including abstract figure at the end)

Description of supplementary material including filename: Supporting information contains additional analyses details and ten supplementary figures, Figure S1–S10. Filename: OCP_SI_ProteinSci_3.docx

This article has been accepted for publication and undergone full peer review but has not been through the copyediting, typesetting, pagination and proofreading process which may lead to differences between this version and the Version of Record. Please cite this article as doi: 10.1002/pro.4273
Received: Sep 21, 2021;Revised: Dec 13, 2021;Accepted: Jan 03, 2022

ABSTRACT

The Orange Carotenoid Protein (OCP) is responsible for nonphotochemical quenching (NPQ) in cyanobacteria, a defense mechanism against potentially damaging effects of excess light conditions. This soluble two-domain protein undergoes profound conformational changes upon photoactivation, involving translocation of the ketocarotenoid inside the cavity followed by domain separation. Domain separation is a critical step in the photocycle of OCP because it exposes the N-terminal domain (NTD) to perform quenching of the phycobilisomes. Many details regarding the mechanism and energetics of OCP domain separation remain unknown. In this work, we apply metadynamics to elucidate the protein rearrangements that lead to the active, domain-separated, form of OCP. We find that translocation of the ketocarotenoid canthaxanthin has a profound effect on the energetic landscape and that domain separation only becomes favorable following translocation. We further explore, characterize, and validate the free energy surface (FES) using equilibrium simulations initiated from different states on the FES. Through pathway optimization methods, we characterize the most probable path to domain separation and reveal the barriers along that pathway. We find that the free energy barriers are relatively small (<5 kcal/mol), but the overall estimated kinetic rate is consistent with experimental measurements (>1 ms). Overall, our results provide detailed information on the requirement for canthaxanthin translocation to precede domain separation and an energetically feasible pathway to dissociation.

KEYWORDS: OCP, domain dissociation, nonphotochemical quenching, cyanobacteria, metadynamics, molecular dynamics simulations

INTRODUCTION

Photosynthetic organisms have developed energy dissipation strategies to prevent damage from the potentially harmful effects of excess light conditions. The Orange Carotenoid Protein (OCP) is a soluble protein with a photoprotective function in cyanobacteria, responsible for nonphotochemical quenching (NPQ) after it is activated by blue-green light.[1–4] This 35 kDa protein consists of two domains connected by an unstructured linker.[5] OCP can bind different carotenoids, including 3'-hydroxyechinenone (3hECN), echinenone (ECN), canthaxanthin (CAN), and zeaxanthin (ZEA).[1] However, the presence of at least one keto group (i.e., 3hECN, ECN, and CAN) is essential for photoactivation.[6] The C-terminal domain (CTD) is a mixed α-helical/β-sheet structure known to act as a "sensor" domain while the N-terminal domain (NTD) has an all α-helical secondary structure, and it is known as the "effector" domain.[7,8] In addition, a short α–helix (αA) in the N-terminal extension (NTE) plays a stabilizing role through interactions with the CTD.[9] Encapsulated between the two domains, the ketocarotenoid interacts with the protein environment through hydrogen bonds and hydrophobic contacts.

The activation mechanism from the inactive orange form (OCP^O) to its active red form (OCP^R) involves a sequence of events, including a 12 Å translocation of the carotenoid into the NTD,[10] triggered by the breakage of the hydrogen bonds that anchor the carotenoid to the CTD in OCP^O, and the dissociation of the two domains in order to expose the domain-interface of the NTD.[11,12] These rearrangements are essential to reach an open conformation necessary to bind the phycobilisomes (PBS), the primary light-harvesting antennae complexes of cyanobacteria.[13–16] The NTD, with the carotenoid in its cavity, is the quencher domain via a close interaction with the PBS. Beyond the desire to uncover the biophysical basis of OCP photoactivation,

understanding the detailed complexity of this system could aid in the design of high-efficiency materials for solar energy capture and storage.

During the OCP^O photoactivation process, the initial events upon excitation occur in picoseconds at a very low quantum yield (~1%), leading to a first red-shifted photoproduct (P1) in which two key hydrogen bonds between the carotenoid and CTD residues Tyr201 and Trp288 are broken. Recent spectroscopy experiments have revealed a series of additional intermediate, red-shifted photoproducts (P2, P2', P3), in which the carotenoid is translocated into the NTD on a timescale of ~10 μs.[17] The next step of the OCP photocycle is the transition from P3 to the fully active OCP^R in which the separation of the two domains occurs on a slow (>1 ms) timescale.[17]

The only available full-length, high-resolution structures of OCP are for the inactive state (OCP^O). While a detailed structural characterization of the dissociated (and other intermediate) state(s) is still elusive, recent X-ray radiolitic labelling analyses of solvent accessibility revealed a series of structural changes, from carotenoid migration to domain separation.[11] Small-angle neutron and X-ray scattering experiments point to rearrangements leading to a flexible 'molten globule' structure of the fully activated OCP^R.[18–20]

The OCP photoactivation process can be divided into three main parts: 1) initial photoactivation of the ketocarotenoid that leads to disruption of key hydrogen bonds, 2) translocation of the ketocarotenoid, and 3) domain dissociation. We (Pigni and Gascón) have recently addressed the second segment of this process by performing translocation of the carotenoid canthaxanthin (CAN) via metadynamics[21] and obtained molecular models of the intermediate photoproducts.[22] This included obtaining a model for OCP-P3, where CAN has

fully migrated into NTD, by matching its spectral signatures to experimental measurements. As stated above, spectroscopy studies suggest that carotenoid translocation (formation of OCP-P3) is relatively slow (~10 μs). However, separation of the domains (OCP-P3 to OCP^R) occurs on a timescale multiple orders of magnitude slower than CAN translocation (> 1 ms).[17] Classical molecular dynamics (MD) simulations are well suited to explore configurations within a local energy minimum and compute ensemble averaged properties. However, to sample across complex energy landscapes with energy barriers significantly exceeding $k_B T$ requires extremely high computational costs and is unlikely to be a feasible approach to obtain meaningful (i.e., converged, statistically significant) results using equilibrium MD. Therefore, applying enhanced sampling methodologies to drive the system away from the local minimum associated with the initial configuration and towards other minima is an advisable approach.[23]

In the present work, we employ well-tempered metadynamics[24] (WT-metaD) to enhance the probability of observing OCP domain separation. In metadynamics, a history-dependent bias potential is built during the simulation as a sum of repulsive Gaussians in the defined collective variables (CVs) space.[21] WT-metaD adds a bias factor (γ) that focus the exploration on physically relevant regions of the conformational space.[24] We explore domain separation from two alternative starting points: the crystal structure of the inactive form, OCP^O (PDB: 4XB5), and our recently published model of the intermediate OCP-P3.[22] Using both OCP^O and OCP-P3 allows us to examine the effect of carotenoid translocation on the energetics of domain separation. A careful definition of two CVs led us to achieve a converged, robust estimate of the free energy surface (FES), which we then utilize to identify the most probable pathway for dissociation and to present a putative model of the fully active OCP^R. A recent study by Bondanza *et al.* utilized umbrella sampling combined with replica exchange molecular dynamics

to study mainly the process of carotenoid translocation in OCP and, with their translocated model of OCP, authors further investigated a qualitative model of domain separation also using WT-metaD.[25]

Our WT-metaD analyses result in a converged FES due to resampling of minima and are validated through equilibrium simulations. We show that dissociation is a thermodynamically favorable process *only* when the carotenoid is translocated, we observe physically meaningful energy barriers (< 5 kcal/mol) along the dissociation pathway, and the overall estimated kinetics is in the range of experimental measurements. Therefore, we present a detailed quantitative analysis of an energetically favorable path for domain separation in OCP.

RESULTS AND DISCUSSION

The NTD and CTD of OCP interact through a major and a minor interface (Figure 1a, b). The major interface is located along a plane approximately orthogonal to the long axis of the carotenoid. The minor interface is composed of interactions between the short α-helix (αA) in the NTE and the CTD β-sheet.[11] Although there is general agreement that carotenoid translocation precedes domain separation,[1,10,17] there is still some debate about the sequence of events that lead to domain separation at the major and minor interfaces.[11,19,26–28] It was initially proposed that conformational changes in the αA occur immediately after the first events of photoactivation, as a consequence of propagation of the rearrangements experienced by the carotenoid.[10,26] On the other hand, based on time-resolved IR spectroscopic studies,[17] it has been suggested that the dissociation of αA occurs on timescales longer than 0.5 ms, preceded by carotenoid translocation and other rearrangements in the NTD, and that such dissociation is a requirement for the complete separation of domains. In general, the hypothesis of the minor

interface's separation preceding the dissociation at the major interface is the most widely accepted.[17,27,28] However, a more recent analysis measuring changes in the solvent accessible areas of particular residues during the OCP photoactivation suggests that the detachment of αA from the CTD could occur after domain separation at the major interface.[11] Here, we examine these questions via enhanced sampling and equilibrium MD simulations and provide a detailed analysis of the structural changes and the path to dissociation.

Free energy surfaces of domain separation in OCP^{O} and OCP-P3

To explore the dissociation of the OCP, we performed two-dimensional WT-metaD simulations. The two CVs were defined to represent the distance between domains at the minor interface (CV1) and at the major interface (CV2). A precise definition of the CVs is shown in Figure 1a, b. The choice of CVs was decided based on the experimental observations that 1) domains must dissociate completely for OCP to later bind the phycobilisome (CV2) and that 2) the NTE helix must also dissociate at some point (CV1) during the photocycle.[10,17,27]

The use of CVs provides a means to project a high dimensional free energy surface onto a small set of variables that can be easily interpreted. The definition of CVs can be a challenge and is an open area of research. However, there are often cases where characteristics of the functionally relevant states are known and CVs can be developed which separate those states along a given set of CVs. Furthermore, there may be experimentally derived kinetic information that supports a given CV as being a "slow" variable. Our choices of CVs are well informed from experimental data and satisfy the conditions of i) separating functionally relevant states, ii) describing slow processes and iii) CV1 and CV2 are non-overlapping (i.e. orthogonal) variables. Nonetheless, there may be limitations in our approach as there may be slow degrees of freedom (other than CV1 and CV2) which are not fully sampled. While our metaD simulations display

good metrics of convergence (Figure S1) other variables we did not consider, such as orientational/rotational variables, are potentially valuable in understanding this transition and could be considered in future work.

To assess the effect of carotenoid translocation on domain separation, we performed the same metadynamics procedure starting from two alternative structures: OCP^O (the inactive OCP) and OCP-P3, a model of the intermediate photoproduct with the carotenoid fully translocated into the NTD (obtained in our previous work).[22] The resulting FESs are shown in Figure 1b, f. The substantial energetic differences between the FESs of OCP^O and OCP-P3 indicate that carotenoid translocation has a profound effect on domain dissociation energetics. Most notably, the global-minima are located at considerably different CV2 values suggesting that domain separation is thermodynamically favored in OCP-P3, and it is not favored in OCP^O (Figure 1b, f). We also projected the 2D FESs onto each CV (Eq. 2 in Methods) to generate 1D profiles (Figure 1c–d, g–h). The projection onto CV2 indicates that the global minimum for OCP^O is at CV2 ≈ 29 Å (Figure 1c), similar to the initial CV2 value (see Table 1 in Methods). In contrast, the FES for OCP-P3 has a broad minimum in CV2 ranging from ~36–40 Å, indicating a domain separation of ~10 Å (Figure 1g). Thus, our FES calculations clearly show that carotenoid translocation precedes domain separation during OCP photoactivation, consistent with UV-vis and IR spectroscopic experiments.[17] Note that the FES in OCP^O presents a global minimum at CV1 ~45 Å (Figure 1b, d), rather than the starting conformation at ~10 Å. However, the local minimum at ~10 Å, which is close to the reference crystal structure, is within 2 kcal/mol from the global minimum. This suggests that the dark state is at equilibrium with other conformations where αA fluctuates between compact and extended states. While crystal structures have only

revealed the compact conformation with αA attached to the CTD, crystallization conditions could have biased the experimental systems towards the αA-CTD associated state.

Recent work by Bondanza *et al*. produced some important insights into domain dissociation in OCP.[25] In their work, the authors investigated OCP domain dissociation before and after carotenoid translocation into the NTD. In the carotenoid translocated state (i.e. OCP-P3) their WT-metaD simulations generated domain separation, whereas OCP-O did not dissociate. While their work revealed new insights into OCP domain dissocation, their WT-metaD simulations did not resample the initial state. This non-ergodic sampling resulted in a FES with non-physical energetic barriers for the dissociation process (~70–90 kcal/mol) even when the carotenoid is translocated. Moreover, regardless of the carotenoid position, their global free energy minimum was the domain-associated state. In contrast, the FESs obtained from our simulations exhibit convergence, state-recrossing events (Figure S1), physically reasonable energy barriers (< 5 kcal/mol), and the prediction of the dissociated state as being thermodynamically favorable only after OCP-P3 formation.

Exploring the free-energy surface at equilibrium

The estimated FESs from WT-metaD can be highly sensitive to the simulation hyper-parameters, the CV choices, and the simulation times. Following our observation that domain separation is only favorable in OCP-P3, we performed a series of equilibrium MD simulations for selected starting states (A–F) from the FES of OCP-P3 (Figure 1f) to test its reliability. We chose low energy states, high energy states, and what we perceived as a saddle point. For each of these states, we performed four MD simulation replicas of 100 ns each. The equilibrium simulations for each state were combined, and their (CV1, CV2) values were projected onto the FES in

Figure 2a–f. The distributions indicate that the configurational samplings from MD simulations reflect the FES's topology.

The MD simulations for state A (the associated state), which corresponds to the early stages of OCP-P3 formation, show a narrow distribution of CV1 and CV2 values, indicating that the system is trapped in a narrow well (Figure 2a). In contrast, simulations that started near what we perceive as a transition state on the FES (state B) produce wider sampling and show the system "falling back" into state A (Figure 2b**)**. When the input structure represents a configuration from a point after the transition state (state C), the simulations did not return to state A; instead, the simulations sampled configurations from the free-energy basin corresponding to the dissociated state (Figure 2c). The MD samplings for state D (Figure 2d) resemble those at state C in that both simulations sample configurations near the global minimum at the dissociate state (state D). Interestingly, when simulations are initiated from the flat region to the right (higher CV1 values) of the dissociated state basin, the equilibrium MD simulations sample a broad range of the configurational space (Figure 2e), reproducing the shallow, entropically favorable, region of the FES. Finally, a set of MD simulations were started from a structure near the upper limit of CV2 (Figure 2f) which produced a distribution that extends along the narrow valley of the dissociated state. This observation led us to confirm that the wall imposed on CV2 in WT-metaD (see Methods) does not affect the estimation of the FES since none of the equilibrium simulations extended beyond the wall location (the wall was not present in the equilibrium MDs). Overall, these results show that equilibrium MD simulations replicate the features of the FES. Thus, our WT-metaD simulation produced a valid and accurate FES for estimating OCP domain dissociation energetics and dynamics.

Path to domain separation

After the validation of the FES obtained from our WT-metaD simulations, we can now address mechanistic questions such as: What is the most probable path on the FES that leads to domain separation in OCP? What are the structural features of the states along this path? To answer these questions, we estimated the most probable transition path (i.e., minimum free energy path, MFEP) between basins in the 2D FES using the Dijkstra algorithm.[29] Using the Dijkstra program, we calculated the MFEP between the initial OCP-P3 state (state A) and the global minimum (state D). Our results indicate that the MFEP transits through three metastable states, M1, M2, and M3 (Figure 3). The MFEP shows that αA rearrangements (the minor interface, CV1) precede separation of the CTD-NTD (the major interface, CV2), as suggested by several experiments.[17,19,26,27]

The MFEP determined by the Dijkstra algorithm was independently verified by performing 100 Monte Carlo (MC) walks on the FES. Using Monte Carlo, we found that most paths followed the Dijkstra MFEP (Figure S2). Of the 100 MC walks, 86 followed a "rightward" path of initially increasing CV1, consistent with the MFEP, while 14 walks followed a more direct path connecting A with D. It should be noted that of the 86 "rightward" paths, 35 walks did not reach the state D basin but remained trapped in an intermediate state (M2). Therefore, MC generated 65 "reactive" trajectories which transited from state A to state D, and 78% of those paths followed the MFEP (Figure 3), while 22% followed the alternative path.

The changing interactions at the domain interfaces along the MFEP were visualized through contact map analysis of states A, M1, M2, M3, and D and are presented in Figure S3. The first transition along the MFEP from the initial state (A) involves a 3.0 kcal/mol barrier to reach M1, a state in which the NTD-CTD interface remains intact while the αA helix unfolds and

separates from the CTD β-strands (Figure 3). This initial transition is primarily a change along CV1, representing dissociation at the minor interface. A small barrier of 0.7 kcal/mol separates M1 from M2, but drastic changes in the orientation of the CTD relative to the NTD occur in this transition as CV2 evolves toward higher values. The change in the contact maps (Figure S3) from state M1 to M2 is also dramatic, showing virtually all interactions present in the A and M1 states at the major interface are no longer present in M2. The largest barrier along the path (4.8 kcal/mol) separates M2 from M3. Contact map analysis of state M3 (Figure S3) shows interactions between the loop, linking helices αC and αD, and the CTD that are not observed in other states, as well as restoration of contacts between a helix aligned perpendicular to the major interface (αG) and the CTD. As well, during the M2 to M3 transition, the pivoting of the CTD exposes most of the NTD-ligand complex to the solvent. The final transition from M3 to state D requires crossing a small barrier (1.0 kcal/mol), reaching a state with a high CV2 value where the interactions between the NTD and the CTD at the major interface are disrupted.

To compare barrier heights on the FESs between OCP^O and OCP-P3, an MFEP analysis was performed on the OCP^O FES as well (Figure S4). The OCP^O MFEP shows that the energy barrier to escape from state A (8.4 kcal/mol barrier) is much larger than in the case of OCP-P3. Even if that event occurs, there are prohibitive barriers to increase CV2 towards a dissociative state. (Figure S4). The major factor contributing to the alteration of the FESs and MFEP barriers between OCP^O and OCP-P3 is the nature in which the carotenoid is interacting with the OCP domains. In OCP^O, the interactions of the ligand are perfectly balanced between the NTD and CTD (Figure S5). In contrast, after translocation, the ligand in OCP-P3 interacts predominantly with the NTD (Figure S5), which indirectly decreases the barriers for dissociation. Thus, we

view the carotenoid ligand acting as a reinforcing "bolt" between the CTD and NTD in OCP^{O}, increasing the barriers for domain separation.

With a detailed characterization of the barriers at hand, we can now examine the kinetics of domain separation for OCP-P3. The MFEP for domain dissociation has two significant free energy barriers $\Delta G_1^{\ddagger}$ = 3.0 kcal/mol and $\Delta G_2^{\ddagger}$ = 4.8 kcal/mol (Figure 4). A simple kinetic analysis based upon a consecutive reaction scheme,

$$\mathrm{A} \xrightarrow[\Delta G_1^{\ddagger}]{k_1} \mathrm{M2} \xrightarrow[\Delta G_2^{\ddagger}]{k_2} \mathrm{D}, \qquad \text{Sch. 1}$$

results in the overall rate $k_{\mathrm{ov}} = k_1 k_2/(k_1 + k_2)$. By applying transition state theory, we can estimate the rate constants from the free energy barriers as $k_i = \omega_i e^{-\Delta G_i^{\ddagger}/k_{\mathrm{B}}T}$; and by assuming that the pre-exponential factors are equivalent ($\omega_1 = \omega_2 = \omega$), the overall rate is given by

$$k_{\mathrm{ov}} = \omega \frac{e^{-\frac{\Delta G_1^{\ddagger} + \Delta G_2^{\ddagger}}{k_{\mathrm{B}}T}}}{e^{-\frac{\Delta G_1^{\ddagger}}{k_{\mathrm{B}}T}} + e^{-\frac{\Delta G_2^{\ddagger}}{k_{\mathrm{B}}T}}}. \qquad \text{Eq. 1}$$

While the value of ω is well-defined for chemical reactions, it is considerably more ambiguous for biomolecular configurational changes, where it represents a barrier crossing attempt frequency. Protein folding literature indicates that $\omega \sim 10^6$ s^{-1} provides a reasonable general estimate.[30,31] Using this estimate for ω, at a temperature of 300 K, the timescale for domain dissociation from OCP-P3 ($\tau = 1/k_{\mathrm{ov}}$) along the MFEP is $\tau \sim 3$ ms. This estimate for domain dissociation occurring at a millisecond timescale is in agreement with a previous study using mid-IR spectroscopy.[17] The precise value of ω is not known for dissociation of protein domains and therefore we also considered a broader range of values that have been estimated from studies on the kinetics of folding small (~80 residue) proteins. From those studies ω is predicted to lie in

the range of 2.5×10^{6} s^{-1} – 10^{5} s^{-1}.[32] Using those values and our computed free energy barriers we estimate OCP-P3 domain dissociation to occur between 1 ms – 30 ms.

The activated state (OCP^{R})

Our proposed path from the OCP-P3 intermediate to a putative model of OCP^{R} is in agreement with several experimental reports that show that the overall secondary structure of each domain is stable during the transition from OCP^{O} to OCP^{R}.[10,19,27,28] In particular, Gupta *et al.* carried out circular dichroism (CD) studies that indicated only a small decrease (~2 %) in the α-helical content for OCP^{R} compared to OCP^{O}, a change that is generally attributed to the unfolding of αA.[19] However, while the structures of the domains undergo minimal perturbations during activation, the interdomain interactions and relative orientation experience significant changes. Interdomain changes have been revealed by small-angle X-ray scattering (SAXS), showing a marked increase in the radius of gyration (R_g) for the activated form of OCP,[19] and chemical cross-linking studies have indicated dramatic changes in the relative orientation of the domains along the photoactivation process.[12] Our simulations are consistent with these experimental findings in that we observe drastic changes in the relative NTD-CTD orientation (e.g., domain pivoting). At the same time, the low intrinsic RMSD values (< 2.5 Å) of each domain along the entire WT-metaD simulation (Figure S6) indicate that the structural integrity of the domains is maintained throughout the path, consistent with CD measurements. Furthermore, despite the low RMSD values of individual domains during activation, our model of the activated state (state D) displays greater structural fluctuations compared with OCP^{O} (Figure S7a). The average RMSF per residue in the entire OCP^{O} is 0.84 Å; in contrast, the average in OCP^{R} (state D) is 2.82 Å. This observation can be attributed to multiple factors, but the RMSF increase in OCP^{R} is likely dominated by the dissociation of the domains. The activated state of OCP has been referred to as

a molten globule-like structure,[20,33] indicating a lack of well-packed tertiary contacts and increased internal dynamics. In addition to the overall increased RMSF values of the activated state we also observe increased internal dynamics in the CTD in OCP^R compared to OCP^O (Figure S7b). These higher internal domain RMSF values for the CTD may result from ligand translocation into the NTD, and correlate with the experimental observations of OCP^R displaying increased dynamics. Another interesting aspect to point out is that as a byproduct of domain separation, the two domains rotate with respect to each other considerably. Figure S8 shows rapid and large rotational fluctuations occurring during the metadynamics trajectory. These fast rotational changes suggest readily accessible rotational states with low energetic barriers separating these states.

According to our FEP results, the activated OCP can be characterized as a dynamic structure fluctuating among different orientations in solution. The finding of an extended global minimum in our FES, together with the wide distribution of configurations explored in the equilibrium MD simulations, particularly starting at advanced states of domain separation (Figure 2c-f), indicate that OCP^R is highly flexible. Once the main interactions between the two domains are disrupted, the flexible nature of the linker (25–30 residues) sustains this enhanced conformational freedom. Indeed, from results of chemical cross-linking studies comparing the inactive and the active forms of OCP, Liu *et al.*[12] proposed that the loop between the two domains allow multiple orientations of NTD and CTD in solution. From our analysis in Figure S8, we suggest that such orientations correspond to rapid and large relative rotations between the domains. In turn, interactions with other proteins, such as the PBS or the fluorescence recovery protein (FRP), are likely to stabilize biologically relevant configurations *in vivo*.

A detailed analysis of the dissociated state can be obtained from the equilibrium MD simulations at the global minimum of OCP-P3 (state D). Figure 5a shows a representative configuration of state D, highlighting the presence of water between the separated domains at the major interface. In general, solvent molecules are known to play an important role in the OCP photoactivation process.[11,19,28] Once OCP domains are dissociated, the carotenoid and the internal face of the NTD are expected to be more exposed to solvent to interact with the PBS complex. Experimental evidence indicates a larger number of water molecules bound to the protein surface in OCP^R.[33] In our simulations, OCP^R (represented by state D) shows increased SASA values for the protein and the ligand when compared to the "closed" state, OCP-P3 (state A). Figure 5c shows that state D reaches ligand SASA values of ~140–150 $Å^2$ during the equilibrium MD simulations. Interestingly, simulations from our previously published work,[22] revealed ligand SASA values of ~39 $Å^2$ for OCP^O, similar to the values observed here for OCP-P3. On the other hand, ligand SASA values for the red carotenoid protein (RCP), which consists only of the isolated NTD, were around 147 $Å^2$.[22] Altogether, these results suggest that our model of OCP^R (state D) can reach levels of ligand solvent exposure similar to the isolated NTD during unbiased equilibrium MD simulations.

Finally, a closer look to the protein interactions in our model of OCP^R shows that, besides the disruption of the secondary helical structure of the NTE at early stages of domain separation observed in our results (M1, Figure 3), the NTE establishes close contacts with different parts of the protein along the pathway of domain dissociation. In particular, a network of hydrogen bonds maintains several NTE-CTD interactions in the activated state (Figure 5b). Some of these interactions are highly conserved during the MD simulations (Figure 5d). Frequently explored conformations of this dynamic state show the NTE interacting with residues at the major

interface, as shown by the contacts of ARG9, which interacts with GLU244 through a salt bridge (~30% frequency) and with GLN228 through a hydrogen bond with an occurrence exceeding 50% (Figure 5d). In addition, the structural proximity between the loop and the domains is also observed in our model (Figure 5e). Interestingly, there is a general agreement between our findings and chemical cross-linking experiments, which have also demonstrated structural proximity between the NTE, the loop, and the CTD in the activated OCP^R.[12] Liu *et al.* have attributed a key role to the linker loop and the NTE, which act as a "structural buffer system" to facilitate the back and forth conversion between OCP^O and OCP^R during the photocycle.[12] The crucial role of the linker in the back-conversion has also been suggested by phylogenetic and mutagenesis analyses.[34] Thus, our observations of the dynamic interactions between the loop and the NTE, keeping the proximity between the two domains, is in line with experimental observations.

CONCLUSIONS

Through the use of equilibrium MD and metadynamics simulations, we have revealed, for the first time, an energetically favorable path to domain separation in OCP. We have presented a quantitative explanation on why translocation of the ketocarotenoid canthaxanthin into the NTD is a prerequisite for a thermodynamically favorable domain dissociation pathway. Furthermore, our calculated free energy surfaces show that the translocation of the ketocarotenoid not only affects the location of the global minimum, it also considerably decreases the energy barriers for domain dissociation. The energy barriers we observe along the minimum free energy pathway (Fig. 4) are surmountable at physiological temperatures, and kinetic analysis predicts a rate of domain dissociation of ~3 ms, in agreement with experimental measurements. The most probable path to domain separation reveals that the detachment of the αA from the β-strands at the minor

interface precedes the disruption of interactions at the major interface. In agreement with experimental data, we propose a dynamic and flexible model for OCP^R that can fluctuate among different conformations in solution. It is highly probable that the interaction with other proteins *in vivo* (i.e., PBS, FRP) could help stabilize the biologically relevant conformations.

While our observations are well supported by agreements with known experimental data, this work also provides predictions about both the mechanism of dissociation and the molecular details of the activated state (OCP^R), which could be further tested experimentally. For example, we predict αA dissociation should precede domain separation; however, we do observe an alternative, less frequent, pathway which does not require αA dissociation. Additionally, we identify key interactions between αA and the CTD, as well as interactions between the domain linker and the domains. In particular, high probability salt bridges are identified (e.g., E174-R239, R9-E244), which could be disrupted through charge reversal mutations. We predict that disruption of these interactions would also affect the efficiency of the OCP photocycle. In summary, our work provides resolution of long standing questions regarding mechanistic details of OCP activation, and generates new avenues for experimental and theoretical exploration.

METHODS

System preparation

Two systems were constructed using Maestro (Schrödinger 2019-3) to model the OCP^O and OCP-P3 states, both containing the carotenoid ligand canthaxanthin. The protein and ligand coordinates for OCP^O were taken from the X-ray crystal structure of OCP^O (PDB: 4XB5), and the coordinates for OCP-P3 were taken from our previously published work.[22] The Protein Preparation application was used to preprocess the protein-ligand complex, assigning bond

orders and adding hydrogens. For the alternative positions of side chains reported in the crystal structures, the most populated ones were used. Optimization of hydrogen bond assignment was performed with default parameters (pH 7.0), and an energy minimization for hydrogens only. The protein was solvated in a cubic box of dimensions 126 Å × 126 Å × 126 Å using the TIP3P water model;[35] the solvated system contained 64,865 molecules. The system was neutralized and modeled with a physiological concentration of salt (0.15 M NaCl), by adding 188 Na^+ and 181 Cl^- ions. All minimizations and MD simulations used the force field OPLS3e.[36]

Before performing production MD or WT-metaD simulations, the systems were relaxed using a multi-stage protocol that included a minimization and short MD simulations. After energy minimizations, the systems were relaxed using the following protocol. (1) NVT with Brownian dynamics at T = 10 K for 100 ps with solute (protein and ligand) atoms restrained. (2) NVT using Langevin thermostat with T = 10 K for 12 ps with solute atoms restrained. (3) NPT using a Langevin thermostat and a Langevin barostat with T = 10 K and a pressure of 1 atm for 12 ps with solute atoms restrained. (4) NPT using a Langevin thermostat and a Langevin barostat with T = 300 K and a pressure of 1 atm for 12 ps with solute atoms restrained. (5) Lastly, simulation in the NPT ensemble using a Langevin thermostat and a Langevin barostat with T = 300 K and a pressure of 1 atm for 1000 ps without restrains.

MD and WT-metaD simulation details

Simulations were run on Nvidia GPU hardware with Desmond[37] (Schrödinger 2019-3). All simulations were run in the NPT ensemble (300 K, 1 atm) using Nosé-Hoover chain and Martyna-Tobias-Klein methods.[38] The time step for the simulations was 2.0 fs. The particle mesh Ewald (PME) method[39] was used for long-range electrostatic interactions with a real space cutoff radius of 9.0 Å. WT-metaD simulations were performed for OCP^O and OCP-P3 systems, using

two CVs to drive domain separation. CV1 is defined as the distance between the centers of mass (COM) of the αA helix (residues 5–9) and the CTD β-strands (residues 222–224, 230–232, 289–291, 299–300. CV2 is defined as the distance between the COM of the NTD (residues 21–160) and the CTD (residues 195–306). The CVs are graphically depicted in Figure 1a, b. An upper limit wall of 65 Å was set for CV1, and an upper wall of 45 Å was set for CV2. The width of the Gaussian potential was σ = 0.8 Å, the initial height W_0 = 1.0 kcal/mol, the deposition time was Δt = 0.1 ps, and the WT-metaD term $k_B \Delta T$ = 5.0 kcal/mol. The total time for each WT-metaD simulation was 500 ns. In the WT-metaD simulation on OCP^O, a restraint was imposed to maintain CAN-CTD interactions while the potential bias was applied to separate the domains (CV1, CV2). Since the hydrogen bonds between CAN and Tyr201/ Trp288 define OCP^O, CAN was restrained to CTD via the hydrogen bond with Trp288. Specifically, a flat-bottomed restraint was applied to the hydrogen bond between Trp288 and CAN using a force constant of 2.0 kcal mol^{-1} $Å^{-2}$, a reference bond length of 1.9 Å, and a tolerance value of 0.2 Å. In a preliminary work, we had found that the absence of the CAN-CTD restraint prevented domain re-association and led to non-ergodic sampling and non-converged FES estimates. A similar restraint was not required for OCP-P3 because CAN is fully embedded in the NTD and domain re-association could be readily achieved.

Based on the free energy surface of OCP-P3, selected regions of the free energy surface were explored using 100 ns equilibrium MD simulations performed in quadruplicate for the equilibrium simulations in Figure 2. The structures used as initial states for these classical MD simulations are shown in Figure S9, superimposed to the crystal structure of OCP^O (PDB ID: 4XB5) to provide an idea of the changes observed along the WT-metaD. The structures are aligned using the NTD as the reference and the corresponding RMSD values are provided. The

same parameters that were used for WT-metaD were used for MD (excluding the WT-metaD specific parameters). A list of all simulations performed is provided in Table I.

FES and dissociation path calculations

The FESs for OCP^O and OCP-P3 were computed using 51 bins for each CV, producing a grid spacing of 1.2 Å along CV1 and 0.4 Å along CV2. Following 500 ns WT-metaD simulations, FESs were produced by Desmond. We monitor The Methjoded the convergence of the WT-metaD simulations by several metrics presented in Figure S1. These convergence metrics include resampling of local and global minimum (i.e. ergodicity) (Figure S1a, b), ΔΔG between initial and global minimum states (Figure S1c, d) and 1-D FES projections (Figure S1e–h). 1D FES profiles were computed by the Boltzmann weighted averaging according to Eq. 2

$$\mathrm{G}(CV_i) = \; -k_\mathrm{B}T\ln \frac{\int e^{-G(CV_i, CV_j)/k_\mathrm{B}T} dCV_j}{\iint e^{-G(CV_i, CV_j)/k_\mathrm{B}T} dCV_i dCV_j} \qquad \text{Eq. 2}$$

where k_B is Boltzmann's constant, T is the system temperature and $\mathrm{G}(CV_i, CV_j)$ is the two-dimensional FES. Additionally, to assess the convergence in estimating the FESs, the standard error of the mean (SEM) was computed using ten-time blocks (block length = 10 ns) over the last 100 ns of the WT-metaD simulations. The corresponding errors are included in Figure 1c–d, g–h.

Minimum free energy path (MFEP). The MFEP connecting the associated (A) and dissociated (D) states on the OCP-P3 FES was computed using the graph theoretical Dijkstra algorithm[29], which has been shown to be an efficient algorithm to find the true MFEP.[40] The Dijkstra algorithm finds the shortest paths between nodes on a graph. In this work, we used a modified version of the algorithm, written in Python programming language, that locates the shortest path

between states on the energy surface. The Dijkstra algorithm was implemented in an in-house python script based on the code by G. Bouvier.[41] Representative structures for the metastable (states M1-M3) and global minimum (state D) states were determined by pooling structures in a small range of CV values around each minimum. The structure with the lowest summed RMSD to all the other locally pooled configurations was chosen as the representative structure for that state. Further details on determining the representative structures can be found in Figure S10.

Monte Carlo sampling. The MFEP obtained via the Dijkstra algorithm was independently verified by performing 100 Monte Carlo walks using the Metropolis criterion at T = 300 K. Trial moves were accepted or rejected according to the probability $\min\{1, \exp(-\Delta G/k_B T)\}$.The FES was interpolated and discretized into a grid of 0.1 Å in CV1 and 0.03 Å in CV2. Each MC walk consisted of 10,000 moves over this grid with a step size of 0.2 Å in the CV1 direction and 0.06 Å in the CV2 direction.

ACKNOWLDGMENTS

This work was supported by the National Science Foundation, award CHE-1904700 (to J.A.G) and the National Institutes of Health through grant number R35-GM119762 (to E.R.M.). Computational resources for this work have been provided through the University of Connecticut Storrs HPC center.

AUTHOR CONTRIBUTIONS

Writing original draft: M. S. and N. P.; Conceptualization, Formal analysis, Methodology, Investigation, Validation, and Writing (review & editing): M. S., N. P., E. M., and J. G.; Funding acquisition, Project administration, Resources, and Supervision: E. M and J. G.;

Visualization: M. S.; Software: M. S., E. M., and J. G.; M. S. and N. P. have contributed equally to this manuscript.

REFERENCES

1. Kerfeld CA, Melnicki MR, Sutter M, Dominguez-Martin MA (2017) Structure, function and evolution of the cyanobacterial orange carotenoid protein and its homologs. New Phytol. 215:937–951.

2. Kirilovsky D, Kaňa R, Prášil O Mechanisms Modulating Energy Arriving at Reaction Centers in Cyanobacteria. In: Demmig-Adams B, Garab G, Adams III W, Govindjee, editors. Non-Photochemical Quenching and Energy Dissipation in Plants, Algae and Cyanobacteria. Vol. 40. Advances in Photosynthesis and Respiration. Dordrecht: Springer Netherlands; 2014. pp. 471–501. Available from: http://link.springer.com/10.1007/978-94-017-9032-1_22

3. Muzzopappa F, Kirilovsky D (2020) Changing Color for Photoprotection: The Orange Carotenoid Protein. Trends Plant Sci. 25:92–104.

4. Wilson A, Ajlani G, Verbavatz J-M, Vass I, Kerfeld CA, Kirilovsky D (2006) A Soluble Carotenoid Protein Involved in Phycobilisome-Related Energy Dissipation in Cyanobacteria. Plant Cell 18:992–1007.

5. Kerfeld CA, Sawaya MR, Brahmandam V, Cascio D, Ho KK, Trevithick-Sutton CC, Krogmann DW, Yeates TO (2003) The Crystal Structure of a Cyanobacterial Water-Soluble Carotenoid Binding Protein. Structure 11:55–65.

6. Punginelli C, Wilson A, Routaboul J-M, Kirilovsky D (2009) Influence of zeaxanthin and echinenone binding on the activity of the Orange Carotenoid Protein. Biochim. Biophys. Acta BBA - Bioenerg. 1787:280–288.

7. Leverenz RL, Jallet D, Li M-D, Mathies RA, Kirilovsky D, Kerfeld CA (2014) Structural and Functional Modularity of the Orange Carotenoid Protein: Distinct Roles for the N- and C-Terminal Domains in Cyanobacterial Photoprotection. Plant Cell 26:426–437.

8. Wilson A, Kinney JN, Zwart PH, Punginelli C, D'Haene S, Perreau F, Klein MG, Kirilovsky D, Kerfeld CA (2010) Structural Determinants Underlying Photoprotection in the Photoactive Orange Carotenoid Protein of Cyanobacteria. J. Biol. Chem. 285:18364–18375.

9. Sluchanko NN, Slonimskiy YB, Moldenhauer M, Friedrich T, Maksimov EG (2017) Deletion of the short N-terminal extension in OCP reveals the main site for FRP binding. FEBS Lett. 591:1667–1676.

10. Leverenz RL, Sutter M, Wilson A, Gupta S, Thurotte A, Carbon CB de, Petzold CJ, Ralston C, Perreau F, Kirilovsky D, et al. (2015) A 12 Å carotenoid translocation in a photoswitch associated with cyanobacterial photoprotection. Science 348:1463–1466.

11. Gupta S, Sutter M, Remesh SG, Dominguez-Martin MA, Bao H, Feng XA, Chan L-JG, Petzold CJ, Kerfeld CA, Ralston CY (2019) X-ray radiolytic labeling reveals the molecular basis of orange carotenoid protein photoprotection and its interactions with fluorescence recovery protein. J. Biol. Chem. 294:8848–8860.

12. Liu H, Zhang H, Orf GS, Lu Y, Jiang J, King JD, Wolf NR, Gross ML, Blankenship RE (2016) Dramatic Domain Rearrangements of the Cyanobacterial Orange Carotenoid Protein upon Photoactivation. Biochemistry 55:1003–1009.

13. Harris D, Tal O, Jallet D, Wilson A, Kirilovsky D, Adir N (2016) Orange carotenoid protein burrows into the phycobilisome to provide photoprotection. Proc. Natl. Acad. Sci. 113:E1655–E1662.

14. Jallet D, Thurotte A, Leverenz RL, Perreau F, Kerfeld CA, Kirilovsky D (2014) Specificity of the Cyanobacterial Orange Carotenoid Protein: Influences of Orange Carotenoid Protein and Phycobilisome Structures. Plant Physiol. 164:790–804.

15. Stadnichuk IN, Krasilnikov PM, Zlenko DV, Freidzon AYa, Yanyushin MF, Rubin AB (2015) Electronic coupling of the phycobilisome with the orange carotenoid protein and fluorescence quenching. Photosynth. Res. 124:315–335.

16. Wilson A, Gwizdala M, Mezzetti A, Alexandre M, Kerfeld CA, Kirilovsky D (2012) The Essential Role of the N-Terminal Domain of the Orange Carotenoid Protein in Cyanobacterial Photoprotection: Importance of a Positive Charge for Phycobilisome Binding. Plant Cell 24:1972–1983.

17. Konold PE, van Stokkum IHM, Muzzopappa F, Wilson A, Groot M-L, Kirilovsky D, Kennis JTM (2019) Photoactivation Mechanism, Timing of Protein Secondary Structure Dynamics and Carotenoid Translocation in the Orange Carotenoid Protein. J. Am. Chem. Soc. 141:520–530.

18. Golub M, Moldenhauer M, Schmitt F-J, Feoktystov A, Mändar H, Maksimov E, Friedrich T, Pieper J (2019) Solution Structure and Conformational Flexibility in the Active State of the Orange Carotenoid Protein: Part I. Small-Angle Scattering. J. Phys. Chem. B 123:9525–9535.

19. Gupta S, Guttman M, Leverenz RL, Zhumadilova K, Pawlowski EG, Petzold CJ, Lee KK, Ralston CY, Kerfeld CA (2015) Local and global structural drivers for the photoactivation of the orange carotenoid protein. Proc. Natl. Acad. Sci. 112:E5567–E5574.

20. Maksimov EG, Shirshin EA, Sluchanko NN, Zlenko DV, Parshina EY, Tsoraev GV, Klementiev KE, Budylin GS, Schmitt F-J, Friedrich T, et al. (2015) The Signaling State of Orange Carotenoid Protein. Biophys. J. 109:595–607.

21. Bussi G, Branduardi D Free-Energy Calculations with Metadynamics: Theory and Practice. In: Parrill AL, Lipkowitz KB, editors. Reviews in Computational Chemistry. Hoboken, NJ, USA: John Wiley & Sons, Inc; 2015. pp. 1–49. Available from: http://doi.wiley.com/10.1002/9781118889886.ch1

22. Pigni NB, Clark KL, Beck WF, Gascón JA (2020) Spectral Signatures of Canthaxanthin Translocation in the Orange Carotenoid Protein. J. Phys. Chem. B 124:11387–11395.

23. Bernardi RC, Melo MCR, Schulten K (2015) Enhanced sampling techniques in molecular dynamics simulations of biological systems. Biochim. Biophys. Acta BBA - Gen. Subj. 1850:872–877.

24. Barducci A, Bussi G, Parrinello M (2008) Well-Tempered Metadynamics: A Smoothly Converging and Tunable Free-Energy Method. Phys Rev Lett 100:020603.

25. Bondanza M, Cupellini L, Faccioli P, Mennucci B (2020) Molecular Mechanisms of Activation in the Orange Carotenoid Protein Revealed by Molecular Dynamics. J. Am. Chem. Soc. 142:21829–21841.

26. Liu H, Zhang H, King JD, Wolf NR, Prado M, Gross ML, Blankenship RE (2014) Mass spectrometry footprinting reveals the structural rearrangements of cyanobacterial orange carotenoid protein upon light activation. Biochim. Biophys. Acta BBA - Bioenerg. 1837:1955–1963.

27. Bandara S, Ren Z, Lu L, Zeng X, Shin H, Zhao K-H, Yang X (2017) Photoactivation mechanism of a carotenoid-based photoreceptor. Proc. Natl. Acad. Sci. 114:6286–6291.

28. Mezzetti A, Alexandre M, Thurotte A, Wilson A, Gwizdala M, Kirilovsky D (2019) Two-Step Structural Changes in Orange Carotenoid Protein Photoactivation Revealed by Time-Resolved Fourier Transform Infrared Spectroscopy. J. Phys. Chem. B 123:3259–3266.

29. Dijkstra EW (1959) A Note on Two Problems in Connexion with Graphs. Numer. Math. 1:269–271.

30. Schuler B, Lipman EA, Eaton WA (2002) Probing the free-energy surface for protein folding with single-molecule fluorescence spectroscopy. Nature 419:743–747.

31. Li MS, Klimov DK, Thirumalai D (2004) Thermal denaturation and folding rates of single domain proteins: size matters. Polymer 45:573–579.

32. Kubelka J, Hofrichter J, Eaton WA (2004) The protein folding 'speed limit.' Curr. Opin. Struct. Biol. 14:76–88.

33. Golub M, Moldenhauer M, Schmitt F-J, Lohstroh W, Maksimov EG, Friedrich T, Pieper J (2019) Solution Structure and Conformational Flexibility in the Active State of the Orange Carotenoid Protein. Part II: Quasielastic Neutron Scattering. J. Phys. Chem. B 123:9536–9545.

34. Muzzopappa F, Wilson A, Kirilovsky D (2019) Interdomain interactions reveal the molecular evolution of the orange carotenoid protein. Nat. Plants 5:1076–1086.

35. Jorgensen WL, Chandrasekhar J, Madura JD, Impey RW, Klein ML (1983) Comparison of simple potential functions for simulating liquid water. J. Chem. Phys. 79:926–935.

36. Roos K, Wu C, Damm W, Reboul M, Stevenson JM, Lu C, Dahlgren MK, Mondal S, Chen W, Wang L, et al. (2019) OPLS3e: Extending Force Field Coverage for Drug-Like Small Molecules. J. Chem. Theory Comput. 15:1863–1874.

37. Bowers KJ, Chow DE, Xu H, Dror RO, Eastwood MP, Gregersen BA, Klepeis JL, Kolossvary I, Moraes MA, Sacerdoti FD, et al. Scalable Algorithms for Molecular Dynamics Simulations on Commodity Clusters. In: ACM/IEEE SC 2006 Conference (SC'06). Tampa, FL: IEEE; 2006. pp. 43–43. Available from: 10.1109/SC.2006.54

38. Martyna GJ, Klein ML, Tuckerman M (1992) Nosé–Hoover chains: The canonical ensemble via continuous dynamics. J. Chem. Phys. 97:2635–2643.

39. Darden T, York D, Pedersen L (1993) Particle mesh Ewald: An Nlog(N) method for Ewald sums in large systems. J. Chem. Phys. 98:10089–10092.

40. Fu H, Chen H, Wang X, Chai H, Shao X, Cai W, Chipot C (2020) Finding an Optimal Pathway on a Multidimensional Free-Energy Landscape. J. Chem. Inf. Model. 60:5366–5374.

41. Bouvier G Compute the shortest path on a grid using python. Available from: https://bougui505.github.io/2016/08/31/compute_the_shortest_path_on_a_grid_using_python.html

TABLES

Table I. List of simulations

Name	Type	Initial CV1	Initial CV2	Length	# Trials
OCP^O	WT-metaD	8.2 Å	28.6 Å	500 ns	1
OCP-P3	WT-metaD	8.6 Å	28.8 Å	500 ns	1
OCP-P3 A	Equilibrium MD	7.9 Å	28.7 Å	100 ns	4
OCP-P3 B	Equilibrium MD	16.4 Å	31.2 Å	100 ns	4
OCP-P3 C	Equilibrium MD	16.5 Å	34.8 Å	100 ns	4
OCP-P3 D	Equilibrium MD	17.2 Å	38.1 Å	100 ns	4
OCP-P3 E	Equilibrium MD	24.7 Å	38.2 Å	100 ns	4
OCP-P3 F	Equilibrium MD	16.5 Å	42.6 Å	100 ns	4

FIGURE LEGENDS

Figure 1. The resulting free energy surfaces from WT-metaD simulations of domain separation starting from OCP^O (left panel) and OCP-P3 (right panel). Molecular representations of OCP^O (a) and OCP-P3 (e). The CVs represent the distances between the centers of mass (COM, grey spheres) of different segments of OCP. CV1 represents the distance between the COM of the αA helix and the CTD β-strands residues. CV2 represents the distance between the COM of NTD and CTD. (b) FES for OCP^O and (f) for OCP-P3. Triangles in (b) and (f) denote the initial configurations (orange) and the the global minimum (red). (c, d) 2D-to-1D projections of the FES of OCP^O onto the CVs; (g, h) projections of the FES of OCP-P3 onto the CVs. The standard error of the mean (error bars) was calculated using 10 ns time blocks over the last 100 ns of the WT-metaD simulations.

Figure 2. Probability densities of the CV values of the OCP-P3 domains separation. (a)–(f) Distributions of the CV1 and CV2 values obtained by unbiased equilibrium MD simulations. The distributions (colored) overlay the free energy surface of OCP-P3's domain separation (grey); dark colors denote relatively high probability densities. A red triangle denotes the coordinates (CV1, CV2) associated with the initial state used for the MD simulations. Each distribution was calculated from a set of four 100-ns simulations.

Figure 3. Minimum free energy path (MFEP) of the OCP-P3 domain dissociation. The molecular-surface representations correspond to the common configuration in the states labeled on the free energy surface. On the FES, the wedges denote free energy barriers in units of kcal/mol; the yellow line represents the MFEP.

Figure 4. Free energy barriers along the MFEP of the OCP-P3 domain dissociation. A, the associated state; M2, a metastable state; D, the dissociated state; TS_1 and TS_2, transition states.

Figure 5. Interactions in OCP-state D and solvent-accessibility comparisons. (a) Molecular-surface representation of state D (dissociated state) and molecular representation of water between domains. (b) Molecular representation of the non-covalent interactions between the NTE and CTD in state D. (c) Probability distributions of the solvent-accessible surface area (SASA) for the ligand (CAN) and the NTD in state A (associated state) and state D. SASA values were calculated using a probe with a radius of 1.4 Å. Data for states A and D were sampled from two sets of MD simulations, each set comprising four 100-ns simulations. (d) Time fractions of the major-noncovalent interactions between the NTE and CTD; (e) between the linker and domains.

FIGURES

Figure 1

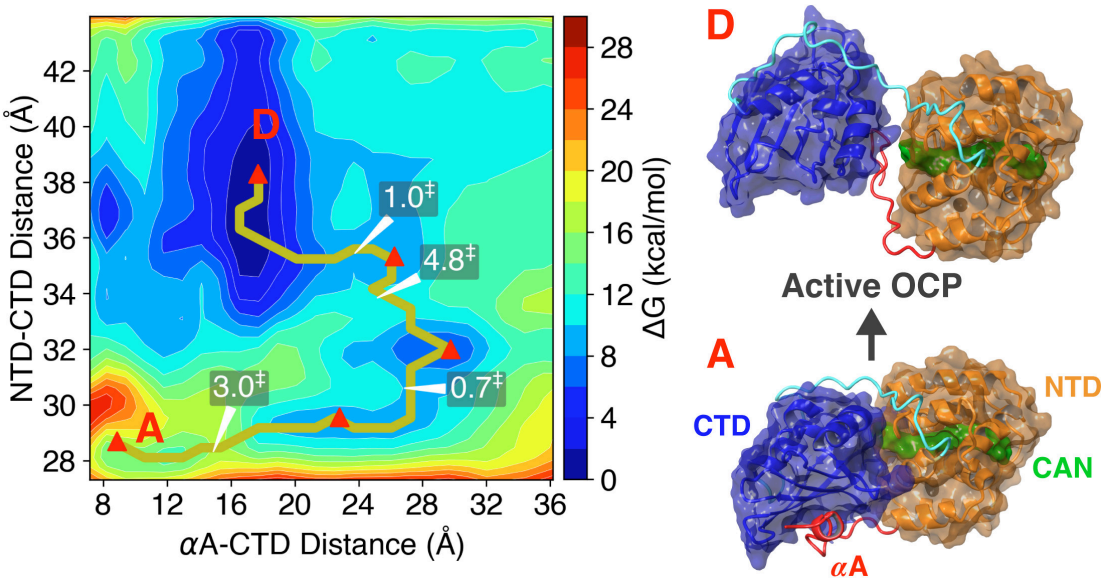

Figure 2

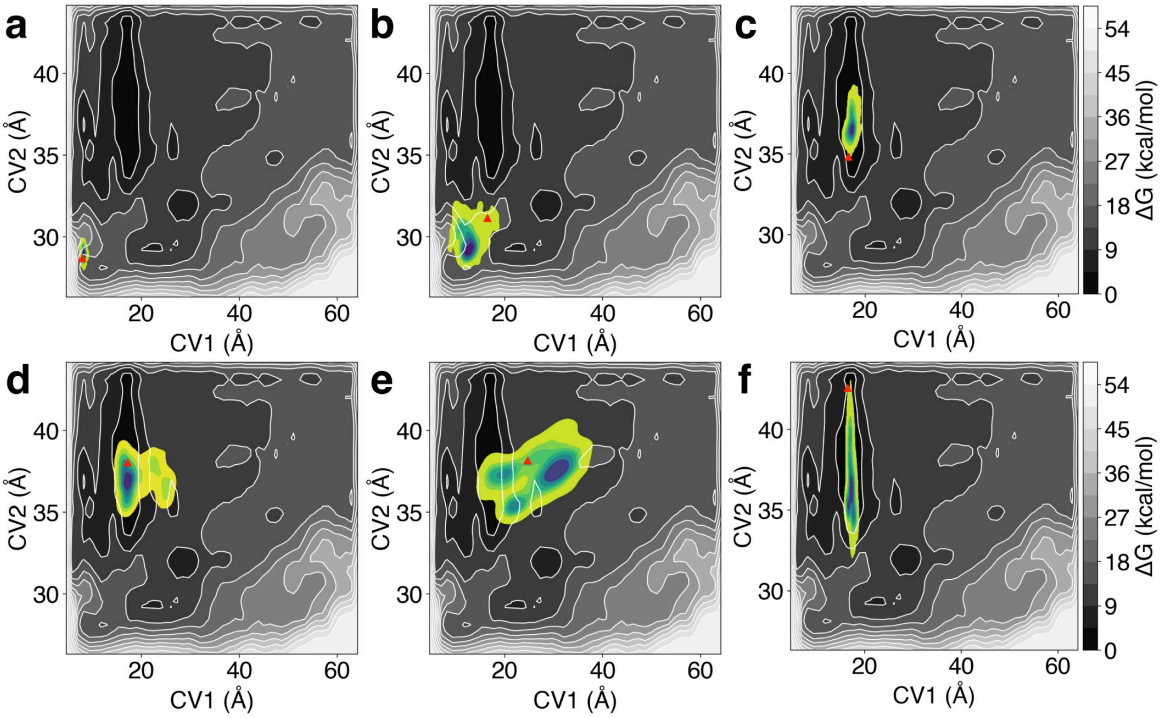

Figure 3

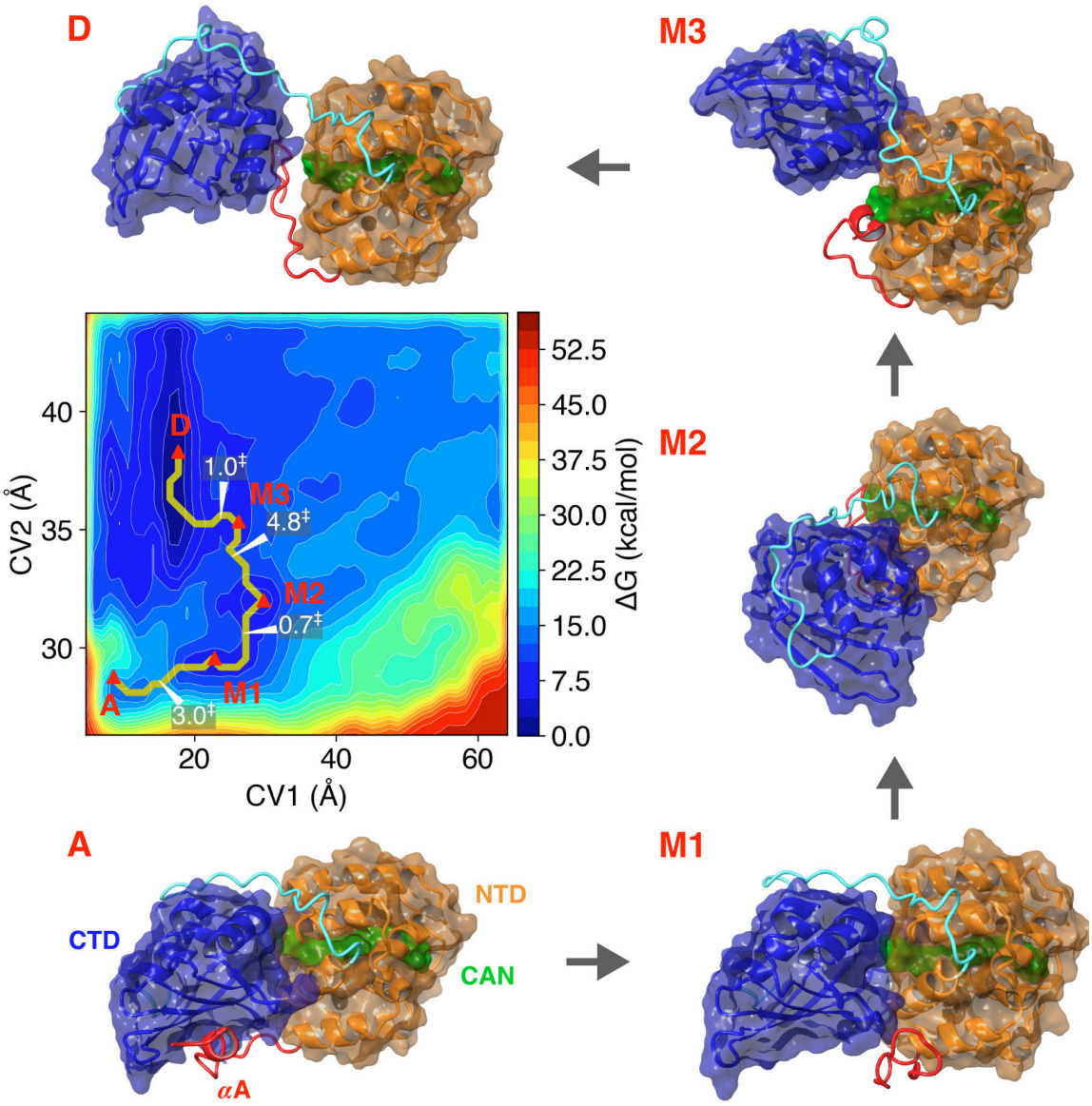

Figure 4

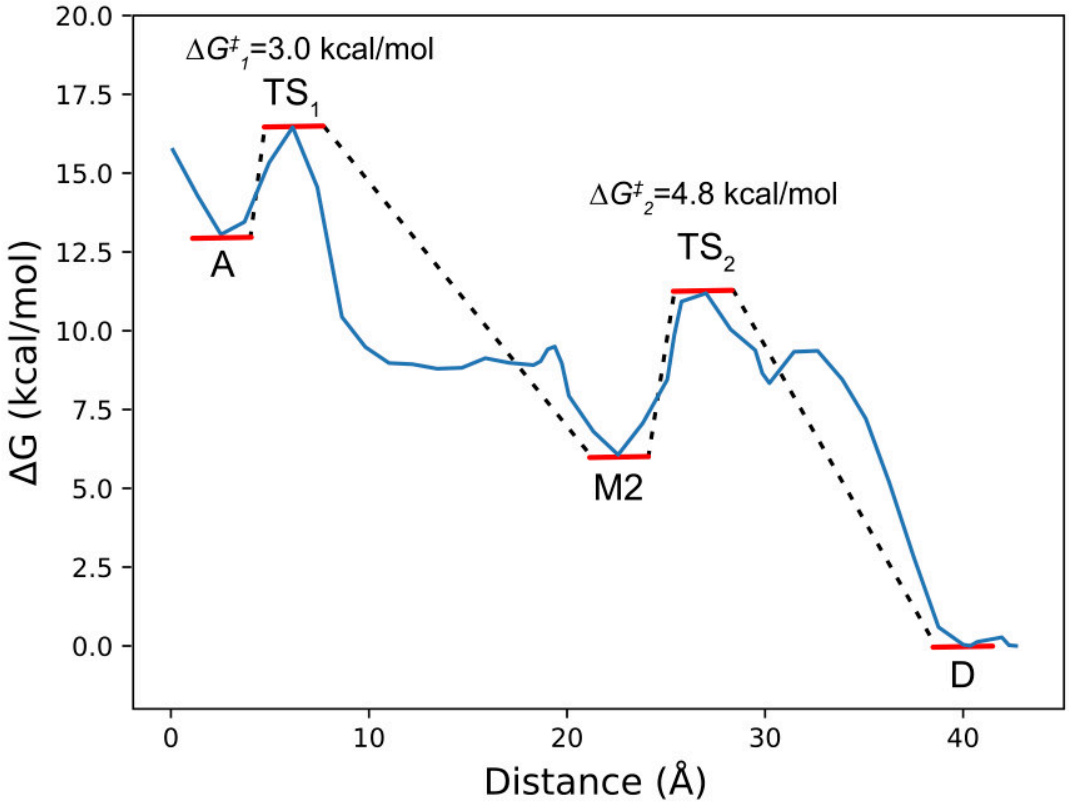

Figure 5